Influence of S and Te substitutions on the thermoelectric properties of the cluster compound Ag3.8Mo9Se11

Philippe Masschelein, Christophe Candolfi, Anne Dauscher, Christine Gendarme, Rabih Al Rahal Al Orabi, Patrick Gougeon, Michel Potel, Philippe Gall, Régis Gautier, B. Lenoir

Influence of S and Te substitutions on the thermoelectric properties of the cluster compound $Ag_{3.8}Mo_9Se_{11}$

P. Masscheleina, C. Candolfia, A. Dauschera, C. Gendarmea, R. Al Rahal Al Orabib,1, P. Gougeonb, M. Potelb, P. Gallb, R. Gautierb, B. Lenoira,*

a *Institut Jean Lamour, UMR 7198 CNRS – Université de Lorraine, 2 allée André Guinier – Campus ARTEM, 54011 Nancy, France*

b *Sciences Chimiques de Rennes, UMR 6226 CNRS – INSA – Ecole Nationale Supérieure de Chimie de Rennes – Université de Rennes 1, Avenue du Général Leclerc, 35042 Rennes, France*

*Corresponding author: bertrand.lenoir@univ-lorraine.fr

1Present address: Advanced Polymers & Materials Department (ARTI/APMD) AXEL'ONE Collaborative Platform - Innovative Materials, 87 rue des frères Perret – BP62, 69192 Saint FONS Cedex. E-mail: rabih.orabi@solvay.com

Abstract

We report on a detailed study of the influence of S and Te substitutions for Se on the thermoelectric properties of the cluster compound $Ag_{3.8}Mo_9Se_{11}$. Two series of polycrystalline samples $Ag_{3.8}Mo_9Se_{11-y}S_y$ ($0 \leq y \leq 0.5$) and $Ag_{3.8}Mo_9Se_{11-z}Te_z$ ($0 \leq z \leq 0.5$) were synthesized by a combination of conventional powder metallurgy technique followed by spark plasma sintering. Powder X-ray diffraction and wavelength dispersive spectroscopy indicate that both S and Te successfully substitute for Se and exhibit a low solubility limit of $y \approx z \approx 0.5$.

Measurements of the thermoelectric properties between 2 and 800 K show that S and Te substitutions tend to lead to a more pronounced heavily-doped character with respect to $Ag_{3.8}Mo_9Se_{11}$. The very low lattice thermal conductivity of these compounds ($\kappa_L \approx 0.5$ W m^{-1} K^{-1}) can be attributed to the large thermal displacement parameters of the Ag atoms. Despite the heavily-doped nature of the samples, the charge carriers conduct less heat than expected by the Wiedemann-Franz law resulting in significantly lower Lorenz numbers than predicted by the degenerate limit above 300 K. The combination of favourable electronic properties and low thermal conductivity leads to interesting dimensionless thermoelectric figures of merit *ZT* of 0.7 near 800 K.

Keywords: reduced molybdenum selenide; molybdenum clusters; thermoelectric properties

1. Introduction

Thermoelectric generators offer a reliable way to convert waste heat into useful electricity without any moving parts or hazardous gas emission [1,2]. The conversion efficiency of thermoelectric materials is quantified through the dimensionless thermoelectric figure of merit $ZT = \alpha^2 T/\rho\kappa$ where T is the absolute temperature, α is the thermopower (or Seebeck coefficient), ρ is the electrical resistivity and κ is the total thermal conductivity [1,2]. Hence, the design of good thermoelectric materials requires achieving a subtle balance between electronic and thermal properties *i.e.* the power factor α^2/ρ should be large while lowering the ability of the material to transport heat.

Compounds with complex crystal structures made of Mo-X (X = S, Se or Te) clusters feature the above-mentioned unusual combination of transport properties and thus, provide a fertile playground to find novel thermoelectric materials [3-16]. The clusters form a three-dimensional network resulting in a large number of atoms per unit cell. The empty space between the clusters can be filled by various metallic atoms, which transfer their electrons to the framework structure. The size and the geometry of the clusters can vary, thereby increasing the structural complexity of the unit cell. Owing to their complex crystal structure, these materials exhibit very low thermal conductivity values as low as ~ 0.5 W m^{-1} K^{-1} above room temperature [11-15]. This property is the key ingredient that leads to moderately high ZT values between 800 and 1100 K [11-15]. The power factor thus appears as the limiting parameter that should be further optimized for enhancing the ZT values.

Our recent investigations on the series $Ag_xMo_9Se_{11}$ ($3.4 \leq x \leq 3.8$) showed that the electronic properties of these *p*-type compounds can be tuned by varying the Ag content leading to promising thermoelectric performances with a peak ZT value of 0.65 at 800 K for x = 3.8 [11,17]. Their crystal structure, shown in Figure 1, is built up by Mo_9Se_{11} cluster units.

The Ag atoms are located in the empty spaces and distributed over four independent crystallographic sites, all of them being partially occupied [6,11]. Based on simple electron counting rules, charge balance is achieved when four electrons are added to the Mo_9 cluster [9,10]. Assuming that Ag is in a +1 valence state, a semiconducting state is therefore predicted to develop for $x = 4$. This picture has been confirmed both experimentally and theoretically, the metallic properties of the $x = 3.4$ compound evolving towards a heavily-doped semiconducting state upon increasing x [9-12]. However, the solubility limit of Ag was found to be slightly lower than $x = 4$ preventing to reach a semiconducting regime [11,12]. In addition, both electrons and holes contribute to the transport which tends to decrease the power factor. Further adjusting the carrier concentration may be a worthwhile route to lessen the detrimental influence of electrons and hence, to enhance the *ZT* values.

One possible way to reach this objective is to envisage substitutions on the Mo and/or Se sites. In Chevrel phases (Mo_6X_8 with X = S, Se or Te), Te and S substitutions for Se lead to modifications in the electronic band structure [18]. These variations influence the carrier concentration giving rise to a more pronounced metallic character of transport [18,19]. Given the structural similarities between these phases and the $Ag_xMo_9Se_{11}$ compounds, it is tempting to posit that these elements will also influence the transport in the $Ag_xMo_9Se_{11}$ series. Herein, we explore two series of polycrystalline samples $Ag_{3.8}Mo_9Se_{11-y}S_y$ ($0 \leq y \leq 0.5$) and $Ag_{3.8}Mo_9Se_{11-z}Te_z$ ($0 \leq z \leq 0.5$) with the aim of determining their influence on the transport properties and assessing the thermoelectric performances of these compounds. using a combination of powder X-ray diffraction, electron probe microanalysis, scanning electron microscopy and transport properties measurements in a broad range of temperatures (2 – 800 K). Among the different compositions experimentally accessible in the $Ag_xMo_9Se_{11}$ system, we chose to restrict our study to $x = 3.8$ since the lowest thermal conductivity values, and hence the highest *ZT*, are achieved at this maximum filling level [11].

2. Experimental details

2.1. Synthesis

Polycrystalline $Ag_{3.8}Mo_9Se_{11-y}S_y$ ($0 \leq y \leq 0.5$) and $Ag_{3.8}Mo_9Se_{11-z}Te_z$ ($0 \leq z \leq 0.5$) samples were synthesized by reacting stoichiometric amounts of Ag (99.999 %, Strem Chemicals), Mo (99.999%, Alfa Aesar) and $MoSe_2$ powders with either $MoTe_2$ or MoS_2 powders. Prior to use, Mo powders were reduced under He/H_2 (ratio 50/50) flowing gas at 1273 K during 3h to avoid the presence of oxygen. The binaries $MoSe_2$, $MoTe_2$ and MoS_2 were prepared from stoichiometric amounts of purified Mo powders, Se (99.999%, 5N+), Te (99.999%, 5N+) and S (99.999%, Alfa Aesar) powders, placed in evacuated and sealed silica tubes, heated at 1073 K and rocked at this temperature for 12h. Both the $Ag_{3.8}Mo_9Se_{11-y}S_y$ and $Ag_{3.8}Mo_9Se_{11-z}Te_z$ series were synthesized at 1323 K for 48h in evacuated and sealed silica tubes. The resulting ingots were ground into fine, micron-sized powders, cold-pressed into pellets and further annealed at 1323 K for 3 days. After a final grinding step, the phase purity was verified by laboratory powder X-ray diffraction prior to consolidation. All the samples were found phase-pure and subsequently, the powders were consolidated by spark plasma sintering (SPS, Dr Sinter 515S, SPS Syntex Inc.) at 1323 K under an uniaxial pressure of 80 MPa during 10 min. Regardless of the starting composition, the density of the resulting cylindrical ingots (~ 12mm diameter, ~ 4mm thick), estimated from their weight and dimensions, was ~ 98% of its theoretical value from crystallographic data. To determine whether the SPS process has led to the formation of side products, the phase purity was further checked by powder X-ray diffraction (PXRD) combined with Rietveld refinements. No secondary phases could be observed in the sulfur-containing samples within the detection limit of PXRD. In contrast, the Te-containing samples showed some secondary phases whose

nature could not be unambiguously identified from the PXRD patterns due to peak overlapping. To ensure a good chemical homogeneity, these samples were subjected to a post-annealing treatment in sealed quartz tubes at 1073 K for one day. The PXRD data collected after this treatment confirmed phase purity.

2.2. Structural and chemical characterizations

Powder X-ray diffraction (PXRD) was carried out to assess phase purity with a Bruker D8 instrument using CuKα_1 radiation. Rietveld analysis of the diffraction patterns was completed using the Fullprof software [20]. Scanning electron microscopy (SEM) in backscattered electron mode (BSE) and X-ray elemental mappings were realized to probe the chemical homogeneity on a Quanta 650 FEG (FEI). In order to determine the actual compositions of the samples, electron probe microanalysis (EPMA) was carried out on polished bulk samples using a JEOL JXA 8530F instrument equipped with wavelength-dispersive spectrometers. The Ag, Mo and Se contents were measured by using the Chevrel phase $AgMo_6Se_8$ as a standard to minimize the experimental error due to absorption phenomena. The concentrations of Te and S were obtained using PbTe and ZnS as standards. The EPMA compositions and the lattice parameters determined from Rietveld refinements against the PXRD data are listed in Tables 1 and 2, respectively. Hereafter, the samples will be labeled by their actual Te and S contents.

2.3. Thermoelectric properties measurements

The SPS-consolidated samples were cut with a diamond wire saw into parts of appropriate shape and size for physical properties measurements. Low-temperature

thermoelectric properties were measured between 2 and 300 K with the thermal transport option (TTO) of a physical property measurement system (PPMS, Quantum Design). The samples, of typical dimensions 2 × 2 × 10 mm^3, were cut perpendicularly to the pressing direction. Our prior work on the $Ag_xMo_9Se_{11}$ samples did not reveal the presence of any significant degree of anisotropy in the transport properties measured parallel and perpendicular to the pressing direction to within experimental uncertainty [11]. The TTO option allows simultaneous measurements of the thermopower, electrical resistivity and thermal conductivity at each temperature. For this measurement, four copper leads were attached onto the samples with conducting silver epoxy to ensure good electrical and thermal contacts. Calibrated cernox thermometers were attached to the sample between 4 and 5 mm apart. The experimental uncertainty associated with measurements of the electrical resistivity and thermopower at low temperatures is estimated to be 5% for each property. For the thermal conductivity, the data are inevitably accompanied by thermal radiations above ~ 200 K which leads to an overestimation of the intrinsic values.

Thermopower and electrical resistivity were measured simultaneously on bar-shaped samples (2 × 2 × 10 mm^3) between 300 and 800 K using a ZEM-3 system (Ulvac-Riko) under partial He atmosphere. Thermal diffusivity a was measured from 300 up to 800 K on a disc-shaped sample (1 mm-thick, 10 mm-diameter) with a LFA-427 instrument (Netzsch). Specific heat C_p measurements were performed in the same temperature range on a DSC 404 F3 apparatus (Netzsch). The total thermal conductivity was then calculated according to the formula $\kappa = aC_pd$ where d is the density, which was considered to be temperature-independent. Except for the low-temperature thermal conductivity data that are obscured by thermal radiations above ~ 200 K, a good match between the low and high-temperature data sets was observed near room temperature. The experimental uncertainty in the measurements of the electrical resistivity, thermopower and thermal conductivity are estimated to be 5%, 5%

and 10%, respectively. The combined uncertainty in the *ZT* evaluation is estimated to be 17 %. Further details about the estimation of the experimental uncertainty on the *ZT* values can be found in Ref. 21.

3. Results and Discussion

3.1. Phase purity

The PXRD patterns for the $y = 0.48$ and $z = 0.47$ samples are shown in Figure 2 (others are provided in the Supplementary data, Figures S1 to S4). All samples crystallize in the orthorhombic space group *Cmcm* of the parent compound $Ag_{3.8}Mo_9Se_{11}$ [6,11,12]. The lattice parameters, determined from Rietveld refinements against the PXRD data, are gathered in Table 2. For the S series, the unit cell volume decreases nearly linearly with increasing the S content probably due to the lower atomic radius of S with respect to Se. In the case of Te, the trend in the lattice parameter is less clear. The unit cell volume first increases slightly for $y = 0.09$ with respect to the parent compound $Ag_{3.8}Mo_9Se_{11}$, in agreement with the larger ionic size of Te with respect to Se. What is more surprising, however, is the monotonic decrease in the unit cell volume upon further increasing the Te concentration up to $z = 0.47$. We note that this trend has been reproduced in two separate batches of samples synthesized by our two groups from different starting products and is thus intrinsic to the present compounds. Our prior investigations on the $Ag_xMo_9Se_{11}$ series have demonstrated that a decrease in the Ag content leads to a decrease in the unit cell volume from 1896.2 $Å_3$ for $x = 3.8$ down to 1887.9 $Å_3$ for $x = 3.4$ [11,12]. The change in the Ag concentration (see Table 1) revealed by EPMA measurements in this series is expected to result in a decrease in the unit cell volume down to about 1894.1 $Å_3$. However, the unit cell volume clearly decreases below this limit in the $z =$

0.26 and 0.47 samples. The evolution of the lattice parameters with the Te content is thus likely not entirely due to the slight change in the Ag concentration as determined by EPMA. Despite the experimental uncertainty in the measurement of the Ag concentration, the transport data are consistent with Ag concentrations higher than $x = 3.6$ and similar in the different samples. A similar trend of the lattice parameters with the Te content has been observed in the Chevrel phases $Mo_6Se_{8-x}Te_x$ for which the c parameters of the hexagonal lattice first decreases up to $x = 1$ before increasing with increasing x up to $x = 8$ [22,23]. This decrease has been attributed to the deformation of the lattice sites of cubic symmetry caused by replacing Te for Se atoms that would push the Te atoms outside their crystallographic sites. Alternatively, previous studies have demonstrated a contraction of the Mo_6, Mo_9 and Mo_{12} clusters when the anionic charge of the $Mo_{3n}X_{3n+2}$ (with $n = 2$, 3 and 4; X = S, Se and Te) increases [7,15,24,25]. Thus, the substitution of Te for Se might induce an increase in the anionic charge of the Mo-Se/Te clusters leading to a concomitant decrease in the size of the clusters and hence, in the lattice parameters.

Due to numerous Se sites in the crystal structure, the position of Te and S atoms could not be reliably determined from these refinements. Within the detection limit of PXRD, no obvious secondary phases are observable up to a substitution level of 0.25 in the S and Te series, respectively (see Figure 2 and Figures S1 to S4 in the Supplementary data). In the $y = 0.48$ and $z = 0.47$ samples, additional reflections assigned to the Chevrel phase $AgMo_6Se_8$ are present. Rietveld refinements with a two-phase model suggest the presence of less than 4 and 2.5 vol% of this impurity phase in the $y = 0.48$ and $z = 0.47$ samples, respectively.

SEM analyses confirm that the samples are phase-pure below $(y, z) < 0.5$. Elemental X-ray maps are shown in Figure 3 for the $y = 0.24$ and $z = 0.47$ samples. With due care due to the overlap of the Kα line of S and Lα line of Mo (2.308 compared to 2.293 eV, respectively), these results indicate that all elements are homogeneously dispersed in the

matrix in the sulfur series. We nevertheless note that for the Te series, these maps reveal the presence of submicrometric precipitates composed of Ag, Te and Se. The fact that such precipitates are detectable suggests that slight differences exist between the nominal and actual Ag and Te contents. EPMA results (Table 1) indeed indicate that the actual Ag and Te concentrations slightly differ from the nominal ones in the Te series while a better correlation between the nominal and actual S contents is observed. Although some slight variations in the Ag content exist between the samples of each series, both series exhibit a similar Ag concentration allowing for a comparison of their transport data.

3.2. Electronic transport properties

Figures 4a and 4b show the $\rho(T)$ data as a function of the temperature for the S and Te series, respectively. Prior studies on the $Ag_xMo_9Se_{11}$ compounds have revealed that the transport properties depend sensitively on the Ag concentration [11,12]. In particular, these compounds have a metallic nature at low Ag contents that evolve towards heavily-doped semiconducting behavior when x varies from x = 3.6 up to 3.9 [11,12]. Here, the reference sample $Ag_{3.8}Mo_9Se_{11}$ behaves similarly with ρ values increasing with temperature above 300 K. At low temperatures, the upturn observed near 100 K has been shown to be related to the presence of holes and electrons, both of which contributing to the electrical conduction in these materials [12].

The influence of Te and S on the ρ data can be qualitatively understood by drawing a parallel between $Ag_xMo_9Se_{11}$ and the Chevrel phases. In the latter family of compounds, several reports have demonstrated that the isovalent substitution of Te for Se reinforces the metallic character of the electrical conduction [18,19]. Although the substitution of S for Se does not change the metallic nature of the compound, it does however lead to variations in the

hole concentration [18,19]. This scenario seems to be equally applicable for the two present series and explains the trend in the electrical resistivity in the Te series, which decreases with increasing the Te content from 25 μΩ m to 10 μΩ m at 300 K on going from $z = 0$ to $z = 0.47$. Of note, the effect of Te on the ρ values outweighs that related to the slight variations in the Ag content observed in this series (see Table 2). The low-temperature upturn observed upon cooling up to $y = 0.24$ disappears for $y = 0.48$. This change in the temperature dependence is likely due to variations in the balance between hole and electron contributions, both carriers being involved in the transport at low temperatures [12].

The overall effect of sulfur (Figure 4a) on ρ is less pronounced than that of Te (Figure 4b) but seems to also lead to lower ρ values. However, a definitive conclusion about the exact influence of Te and S on the electrical properties is difficult to draw. Our prior investigation on the transport properties of the $Ag_xMo_9Se_{11}$ series have shown that both the temperature dependence and the electrical resistivity values are sensitive to the Ag concentration with lower x values tending to increase the heavily-doped character of the transport [11,12]. Our EPMA measurements have indicated some variations in the Ag content from sample to sample, the influence of which on the electrical resistivity might partly counterbalance the influence of S or Te.

Although the variations in the hole concentrations may be tracked by Hall effect measurements, the situation is complicated here by the competition between holes and electrons [12]. In the $Ag_xMo_9Se_{11}$ series, the presence of both types of carriers has been explained by the presence of flat, weakly-dispersive valence bands near the band gap resulting in regions of positive and negative curvatures near the Fermi level [12]. The substitution levels achieved here are likely too low to induce drastic modifications of the electronic band structure. The galvanomagnetic properties in the present series of samples (not shown) are

indeed very similar to those observed in the parent compounds making it difficult to analyze in detail the hole concentration and mobility.

The temperature dependence of the thermopower up to 800 K (Figures 5a and 5b) confirms the trends seen in the $\rho(T)$ data. In the Te series, the positive α values decreases from 70 μV K^{-1} to 40 μV K^{-1} at 300 K with increasing the Te content. The nonlinear temperature dependence of the reference sample, characteristic of a heavily-doped semiconducting behavior, is lessened upon substituting Te for Se and eventually, is no longer visible in the y = 0.47 sample which exhibits a pure diffusive regime coherent with its metallic nature. The substitution of S for Se leaves both the temperature dependence and the measured values of α practically unchanged.

3.3. Thermal transport properties

Figures 6a and 6b show the temperature dependence of the total thermal conductivity for the Te and S series of samples, respectively. With no exceptions, all the samples exhibit a temperature dependence that mirrors that of glassy systems with the absence of an Umklapp peak at low temperatures and a nearly temperature-independent behavior at high temperatures. The very low κ values that range between 0.7 and 1.1 W m^{-1} K^{-1} at 300 K are comparable to those achieved in other Mo-based cluster compounds such as $Ag_2Tl_2Mo_9Se_{11}$ or $Ag_3In_2Mo_{15}Se_{19}$ [13,14] and in other thermoelectric materials that are poor thermal conductors such as Zintl phases, tetrahedrites or chalcogenides [26-36]. Both the high disorder at the Ag sites and the large thermal displacement parameters of the Ag atoms are likely the key ingredients that limit significantly the phonon mean-free path and hence κ_L [6].

In non-magnetic materials and in the absence of bipolar conduction, the total thermal conductivity is the sum of an electronic κ_e and a lattice contribution κ_L. In order to

estimate κ_L, we tried to subtract the electronic part using the Wiedemann-Franz law $\kappa_e = LT/\rho$ where L is the Lorenz number. In metals and degenerate semiconductors, L attains its Sommerfeld value L_0 = 2.45 × 10^{-8} V^2 K^{-2} at temperatures above the Debye temperature θ_D due to the predominance of elastic electron scattering by short-wavelength phonons [37]. Significant departure from this value emerges at low temperatures as a result of inelastic electron scattering processes that outweigh elastic scattering events [37]. In the present series of samples, the rather low ρ values measured combined with the low θ_D values estimated in the Ag$_x$Mo$_9$Se$_{11}$ ($3.4 \leq x \leq 3.8$) compounds (~ 180 K, Ref. 14) suggest that assuming $L \approx L_0$ above 200 K should be an appropriate approximation. However, this simple hypothesis fails to yield a correct estimation of κ_L as it would result in values below 0.1 W m^{-1} K^{-1} near 800 K for Ag$_{3.8}$Mo$_9$Se$_{11-z}$Te$_z$, that is, in κ_L values well below the glassy limit κ_{min} estimated to be 0.45 W m^{-1} K^{-1} above 300 K from the longitudinal and transverse sound velocities measured on the two end-member compounds (y = 0.48 and z = 0.47) [38,39]. κ_{min} represents a natural lower limit that cannot be decreased since, when κ_L reaches κ_{min}, the phonon mean-free path attains its lowest possible value that correspond to half-wavelength of phonons. Hence, considering that κ_L should remain higher than or equal to κ_{min}, this means that L must be significantly lower than the degenerate limit and fall in the range 1.5 – 1.8 × 10^{-8} V^2 K^{-2}. The fact that the degenerate limit is no longer a valid approximation to estimate κ_e at high temperatures has been also observed in several other metallic systems such as the Zintl phases Eu$_9$Cd$_{4-x}$*TM*$_{2+x-y}$□$_y$Sb$_9$ (*TM* = Cu, Ag and Au and □ is a vacancy) or Mo$_3$Sb$_7$ and its ternary and quaternary derivatives [40-47]. In the latter system, the anomalous thermal transport and the unusual evolution upon alloying on the Mo or Te sites have been explained by the strong electron-phonon coupling present in Mo$_3$Sb$_7$ which is progressively suppressed when the substitution level is increased [48,49]. These results suggest that electron-phonon scattering might equally play an important role in the present case. Since the temperature

dependence and the values of the Lorenz numbers depend on the scattering mechanisms, this additional source of diffusion might explain the strong deviations of L from L_0 in these metallic samples above 300 K.

In order to disentangle both contributions to κ, we have followed the procedure used by Kazem *et al.* [40] for $Eu_9Cd_{4-x}TM_{2+x-y}\square_ySb_9$. The Lorenz number has been estimated at 780 K by the expression $L_{estimate} = \frac{(\kappa_{780K}-\kappa_{min})\times\rho(780K)}{780K}$, that is, the lattice thermal transport is assumed to have reached κ_{min} at high temperatures. This hypothesis leads to $L_{estimate}$ values varying between 1.47 – 1.94 × 10^{-8} V^2 K^{-2} and 1.24 – 2.26 × 10^{-8} V^2 K^{-2} for the S and Te series, respectively. We note that the increasing thermopower values, although indicative of temperature-dependent Lorenz numbers, cannot solely explain the lowest values of $L_{estimate}$ obtained for both series. The lattice contribution κ_L has been then obtained following the relation $\kappa_L = \kappa - \frac{L_{estimate}\times T}{\rho(T)}$. Within this approach, L is thus assumed to be temperature-independent and equal to $L_{estimate}$ between 300 and 780 K. As shown in Figures 6c and 6d, the estimated κ_L values are nearly equivalent due to the low substitution levels that do not result in enhanced point defect scattering.

3.4. Dimensionless thermoelectric figure of merit ZT

The temperature dependence of *ZT* is shown in Figures 7a and 7b. Owing to the more metallic character of the substituted samples with respect to $Ag_{3.8}Mo_9Se_{11}$, the *ZT* values are lower in the whole temperature range for the Te series. The weak influence of sulfur on the transport properties does not lead to significant differences in the *ZT* values that remain similar to those of the $Ag_{3.8}Mo_9Se_{11}$ sample within experimental uncertainty. Nevertheless, a maximum *ZT* of 0.7 is reached at 800 K, making these compounds interesting candidates for high-temperature thermoelectric applications. The ability to adjust the carrier concentration in

this system appears essential in further optimizing the *ZT* values. Since the Mo_9Se_{11} clusters seem less flexible than the Mo_6X_8 (*X* = Se, Te, S) clusters of the Chevrel phases for which complete solid solutions exist, substitutions on the Ag sites may be a worthwhile way of research to explore. A preliminary study performed on the $Ag_{3.6}Cu_xMo_9Se_{11}$ compounds (x = 0.2 and 0.4) has indeed indicated the possibility to improve the thermoelectric performances upon introducing Cu [17]. These results suggest that further optimization might be realized by considering either isovalent or aliovalent substitutions for Ag.

4. Summary and conclusion

Partial substitutions of S and Te for Se in the $Ag_{3.8}Mo_9Se_{11}$ cluster compound were successfully realized by a conventional powder metallurgy route followed by spark plasma sintering. Both phases show a narrow compositional range with similar maximum substitution levels of approximately 0.5. The influence of Te mirrors that observed in the Chevrel phases with a more pronounced metallic character as the Te content increases. This naturally explains the detrimental effect of Te on the thermoelectric properties reflected by lower *ZT* compared with the unsubstituted sample. The influence of substituting S for Se is less pronounced compared to Te and does not lead to a significant increase in *ZT* due to the low homogeneity range. Nevertheless, a peak *ZT* of 0.7 at 800 K reached in the y = 0.095 sample suggests that these compounds are interesting *p*-type materials for thermoelectric applications at high temperatures and warrants further investigations.

Acknowledgements

The authors acknowledge the European Space Agency under NPI contract and the French National Agency (ANR MASSCOTE) for financial support.

Notes

The authors declare no competing financial interest.

Appendix A. Supporting Information

Supplementary data associated with this article can be found in the online version at doi:10.1016/j.jssc. (to be completed).

References

[1] *Thermoelectrics and its Energy Harvesting*, ed. D. M. Rowe, CRC Press, 2012.

[2] H. J. Goldsmid in *Thermoelectric Refrigeration*, Temple Press Books, Ltd., London, 1964.

[3] R. Chevrel, M. Sergent, in *Superconductivity in Ternary Compounds I,* Topics of Current Physics Vol. 32, edited by Ø. Fischer and M. B. Maple (Springer, Berlin, Heidelberg, 1982), pp. 25–86.

[4] T. Caillat, J. P. Fleurial, G. J. Snyder, Solid State Sci. 1 (1999) 535.

[5] R. W. Nunes, I. I. Mazin, D. J. Singh, Phys. Rev. B 59 (1999) 7969.

[6] P. Gougeon, J. Padiou, J. Y. Le Marouille, M. Potel, M. Sergent, J. Solid State Chem. 51 (1984) 218.

[7] P. Gougeon, M. Potel, R. Gautier, Inorg. Chem. 43 (2004) 1257.

[8] S. Picard, J.-F. Halet, P. Gougeon, M. Potel, Inorg. Chem. 38 (1999) 4422.

[9] P. Gougeon, M. Potel, J. Padiou, M. Sergent, C. Boulanger, J. M. Lecuire, J. Solid State Chem. 71 (1987) 543.

[10] R. Gautier, P. Gougeon, J.-F. Halet, M. Potel, J.-Y. Saillard, J. Alloys Compd. 262–263 (1997) 311.

[11] T. Zhou, B. Lenoir, M. Colin, A. Dauscher, P. Gall, P. Gougeon, M. Potel, E. Guilmeau, Appl. Phys. Lett. 98 (2011) 162106.

[12] T. Zhou, M. Colin, C. Candolfi, C. Boulanger, A. Dauscher, E. Santava, J. Hejtmanek, P. Baranek, R. Al Rahal Al Orabi, M. Potel, B. Fontaine, P. Gougeon, R. Gautier, B. Lenoir, Chem. Mater. 26 (2014) 4765.

[13] P. Gougeon, P. Gall, R. Al Rahal Al Orabi, B. Fontaine, R. Gautier, M. Potel, T. Zhou, B. Lenoir, M. Colin, C. Candolfi, A. Dauscher, Chem. Mater. 24 (2012) 2899.

[14] R. Al Rahal Al Orabi, P. Gougeon, P. Gall, B. Fontaine, R. Gautier, M. Colin, C. Candolfi, A. Dauscher, J. Hejtmanek, B. Malaman, B. Lenoir, *Inorg. Chem.*, 2014, **53**, 11699.

[15] R. Al Rahal Al Orabi, B. Fontaine, R. Gautier, P. Gougeon, P. Gall, Y. Bouyrie, A. Dauscher, C. Candolfi, B. Lenoir, Inorg. Chem. 55 (2016) 6616.

[16] G. Daigre, P. Gougeon, P. Gall, R. Gautier, O. Guillou, J.-B. Vaney, C. Candolfi, A. Dauscher, B. Lenoir, J. Solid State Chem. 237 (2016) 1.

[17] M. Colin, T. Zhou, B. Lenoir, A. Dauscher, R. Al Rahal Al Orabi, P. Gougeon, M. Potel, P. Baranek, C. Semprimoschnig, J. Elec. Mater. 41 (2012) 1360.

[18] K. Yvon in *Current Topics in Material Science*, Ed. E. Kaldis, Elsevier: North-Holland, Amsterdam, Vol. 3, 1979.

[19] X. Shi, L. Wang, L. Chen, X. Chen, *Trans. Nonferrous Met. Soc. China* 19 (2009) 642.

[20] J. Rodriguez-Carvajal, Physica B 192 (1993) 55.

[21] E. Alleno, D. Bérardan, C. Byl, C. Candolfi, R. Daou, R. Decourt, E. Guilmeau, S. Hébert, J. Hejtmanek, B. Lenoir, P. Masschelein, V. Ohorodniichuk, M. Pollet, S. Populoh, D. Ravot, O. Rouleau, M. Soulier, Rev. Sci. Instrum. 86 (2015) 011301.

[22] R. Chevrel, M. Sergent, Ø. Fischer, Mater. Res. Bull. 10, (1975) 1169.

[23] C. Hamard, V. Auffret, O. Peña, M. Le Floch, B. Nowak, A. Wojakowski, Physica B 291 (2000) 339.

[24] S. Picard, P. Gougeon, M. Potel, Inorg. Chem. 45 (2006) 1611.

[25] D. Salloum, R. Gautier, P. Gougeon, and M. Potel. J. Solid State Chem., 177 (2004) 1672.

[26] S. R. Brown, S. M. Kauzlarich, F. Gascoin, G. J. Snyder, Chem. Mater. 18 (2006) 1873.

[27] S. K. Bux, A. Zevalkink, O. Janka, D. Uhl, S. M. Kauzlarich, G. J. Snyder, J.-P. Fleurial, J. Mater. Chem. A 2 (2014) 215.

[28] U. Aydemir, A. Ormeci, Z. M. Gibbs, S. Bux, G. J. Snyder, Chem. Mater. 27 (2015) 1622.

[29] K. Suekuni, K. Tsuruta, T. Ariga, M. Koyano, Appl. Phys. Express 5 (2012) 051201.

[30] X. Lu, D. T. Morelli, Y. Xia, F. Zhou, V. Ozolins, H. Chi, X. Zhou, C. Uher, Adv. Energy Mater. 3 (2013) 342.

[31] Y. Bouyrie, C. Candolfi, V. Ohorodniichuk, B. Malaman, A. Dauscher, J. Tobola, B. Lenoir, J. Mater. Chem. C 3 (2015) 10476.

[32] Y. Bouyrie, C. Candolfi, S. Pailhès, M. M. Koza, B. Malaman, A. Dauscher, J. Tobola, O. Boisron, L. Saviot, B. Lenoir, Phys. Chem. Chem. Phys. 17 (2015) 19751.

[33] Y. Bouyrie, C. Candolfi, A. Dauscher, B. Malaman, B. Lenoir, *Chem. Mater.* 27 (2015) 8354.

[34] S. Sassi, C. Candolfi, J.-B. Vaney, V. Ohorodniichuk, P. Masschelein, A. Dauscher, B. Lenoir, Appl. Phys. Lett. 104 (2014) 212105.

[35] Q. Zhang, E. Kebede Chere, J. Sun, F. Cao, K. Dahal, S. Chen, G. Chen, Z. Ren, Adv. Energy Mater. 5 (2015) 1500360.

[36] Y. Chen, M. D. Nielsen, Y.-B. Gao, T.-J. Zhu, X. Zhao, J. P. Heremans, Adv. Energy Mater. 2 (2012) 58.

[37] C. Uher in Thermal conductivity, Theory, Properties and Applications, Edited by T. M. Tritt, 2006, p. 21.

[38] D. G. Cahill, S. K. Watson, R. O. Pohl, Phys. Rev. B 46 (1992) 6131.

[39] D. G. Cahill, R. O. Pohl, Annu. Rev. Phys. Chem. 39 (1988) 93.

[40] N. Kazem, J. V. Zaikina, S. Ohno, G. J. Snyder, S. M. Kauzlarich, *Chem. Mater.*, 2015, **27**, 7508-7519.

[41] C. Candolfi, B. Lenoir, A. Dauscher, E. Guilmeau, J. Hejtmanek, J. Tobola, B. Wiendlocha, S. Kaprzyk, Phys. Rev. B 79 (2009) 035114.

[42] J.-Q. Yan, M. A. McGuire, A. F. May, H. Cao, A. D. Christianson, D. G. Mandrus, B. C. Sales, Phys. Rev. B 87 (2013) 104515.

[43] C. Candolfi, B. Lenoir, A. Dauscher, C. Bellouard, J. Hejtmanek, E. Santava, J. Tobola, J. Appl. Phys. 105 (2009) 083701.

[44] C. Candolfi, B. Lenoir, A. Dauscher, J. Hejtmanek, J. Tobola, Phys. Rev. B 79 (2009) 235108.

[45] C. Candolfi, B. Lenoir, A. Dauscher, J. Hejtmanek, J. Tobola, Phys. Rev. B 80 (2009) 155127.

[46] C. Candolfi, B. Lenoir, C. Chubilleau, A. Dauscher, E. Guilmeau, J. Phys. C: Condens. Matter 22 (2010) 025801.

[47] C. Candolfi, B. Lenoir, A. Dauscher, M. M. Koza, M. de Boissieu, M. Sternik, K. Parlinski, Phys. Rev. B 84 (2011) 224306.

[48] X. Shi, Y. Pei, G. J. Snyder, L. Chen, Energy Environ. Sci. 4 (2011) 4086.

[49] D. Bansal, C. W. Li, A. H. Said, D. L. Abernathy, J. Yan, O. Delaire, Phys. Rev. B 92 (2015) 214301.

Table Captions

Table 1

Nominal and actual compositions measured by EPMA for the $Ag_{3.8}Mo_9Se_{11-y}S_y$ and $Ag_{3.8}Mo_9Se_{11-z}Te_z$ series. The chemical formulae were normalized to 9 Mo atoms per formula unit.

Series S		*Series Te*	
Nominal composition	*Actual composition*	*Nominal composition*	*Actual composition*
$Ag_{3.8}Mo_9Se_{11}$	$Ag_{3.73\pm0.13}Mo_9Se_{11.27\pm0.22}$	/	/
$Ag_{3.8}Mo_9Se_{10.9}S_{0.1}$	$Ag_{3.79\pm0.16}Mo_9Se_{10.86\pm0.18}S_{0.095\pm0.007}$	$Ag_{3.8}Mo_9Se_{10.9}Te_{0.1}$	$Ag_{3.81\pm0.17}Mo_9Se_{10.94\pm0.21}Te_{0.09\pm0.008}$
$Ag_{3.8}Mo_9Se_{10.75}S_{0.25}$	$Ag_{3.70\pm0.12}Mo_9Se_{10.80\pm0.11}S_{0.24\pm0.01}$	$Ag_{3.8}Mo_9Se_{10.75}Te_{0.25}$	$Ag_{3.75\pm0.13}Mo_9Se_{10.78\pm0.17}Te_{0.26\pm0.02}$
$Ag_{3.8}Mo_9Se_{10.5}S_{0.5}$	$Ag_{3.71\pm0.12}Mo_9Se_{10.42\pm0.16}S_{0.48\pm0.03}$	$Ag_{3.8}Mo_9Se_{10.5}Te_{0.5}$	$Ag_{3.72\pm0.12}Mo_9Se_{10.65\pm0.18}Te_{0.47\pm0.05}$

Table 2

Lattice parameters and unit cell volume inferred from Rietveld refinements against PXRD data for the $Ag_{3.8}Mo_9Se_{11-y}S_y$ and $Ag_{3.8}Mo_9Se_{11-z}Te_z$ series.

Series S				
y	*a (Å)*	*b (Å)*	*c (Å)*	*V (Å$_3$)*
0.0	11.9098(7)	13.6249(9)	11.6831(7)	1895.8
0.095	11.9045(6)	13.6244(8)	11.6776(6)	1894.0
0.24	11.8946(5)	13.6161(6)	11.6688(5)	1889.9
0.48	11.8841(4)	13.6043(5)	11.6556(4)	1884.4
Series Te				
z	*a (Å)*	*b (Å)*	*c (Å)*	*V (Å$_3$)*
0.0	11.9098(7)	13.6249(9)	11.6831(7)	1895.8
0.09	11.9103(1)	13.6362(1)	11.6853(1)	1897.8
0.26	11.9122(2)	13.6073(3)	11.6716(2)	1892.1
0.47	11.9132(4)	13.5869(5)	11.6695(4)	1888.8

Figure Captions

Fig. 1. Crystal structure of the $Ag_xMo_9Se_{11}$ cluster compounds viewed along the (a) *a* and (b) *b* crystallographic axes. The Mo atoms are in blue, the Se atoms are in red and the Ag atoms are in light grey. The thermal ellipsoids are drawn at the 95% probability level.

Fig. 2. Rietveld refinements of the PXRD patterns for the (a) $y = 0.48$ and (b) $z = 0.47$ samples. The vertical green ticks mark the calculated Bragg reflections of the major ($Ag_xMo_9Se_{11}$, first row) and minority phases ($AgMo_6Se_8$, second row) while the bottom curve corresponds to the residuals of the Rietveld refinement.

Fig. 3. SEM images in backscattered electron mode and elemental mappings for the (a) $y = 0.24$ and (b) $z = 0.47$ samples.

Fig. 4. Electrical resistivity ρ as a function of temperature for the (a) $Ag_{3.8}Mo_9Se_{11-y}S_y$ and (b) $Ag_{3.8}Mo_9Se_{11-z}Te_z$ series.

Fig. 5. Temperature dependence of the thermopower α of the (a) $Ag_{3.8}Mo_9Se_{11-y}S_y$ and (b) $Ag_{3.8}Mo_9Se_{11-z}Te_z$ samples.

Fig. 6. Temperature dependence of the total thermal conductivity κ for the (a) $Ag_{3.8}Mo_9Se_{11-y}S_y$ and (b) $Ag_{3.8}Mo_9Se_{11-z}Te_z$ samples. The lattice thermal conductivity κ_L is shown in panels (c) and (d) for the S and Te series, respectively. The lack of data around 300 K is due to the thermal radiations that accompany these measurements and lead to overestimated κ values. The horizontal solid black line represents the minimum thermal conductivity κ_{min} estimated using the model of Cahill and Pohl (Refs. 34 and 35).

Fig. 7. Dimensionless thermoelectric figure of merit *ZT* as a function of temperature for the $Ag_{3.8}Mo_9Se_{11-y}S_y$ (a) and $Ag_{3.8}Mo_9Se_{11-z}Te_z$ (b) series.

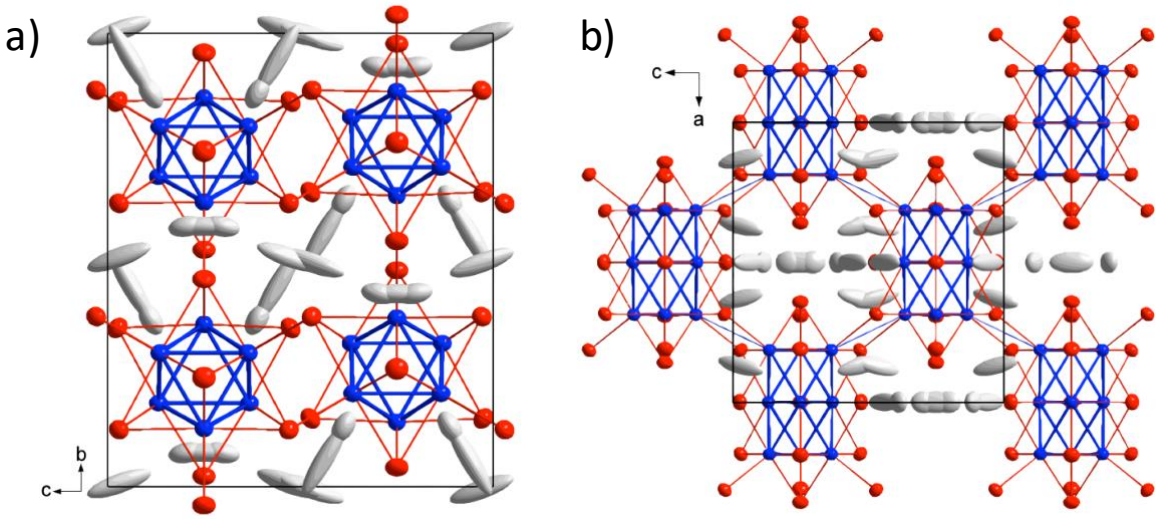

Figure 1

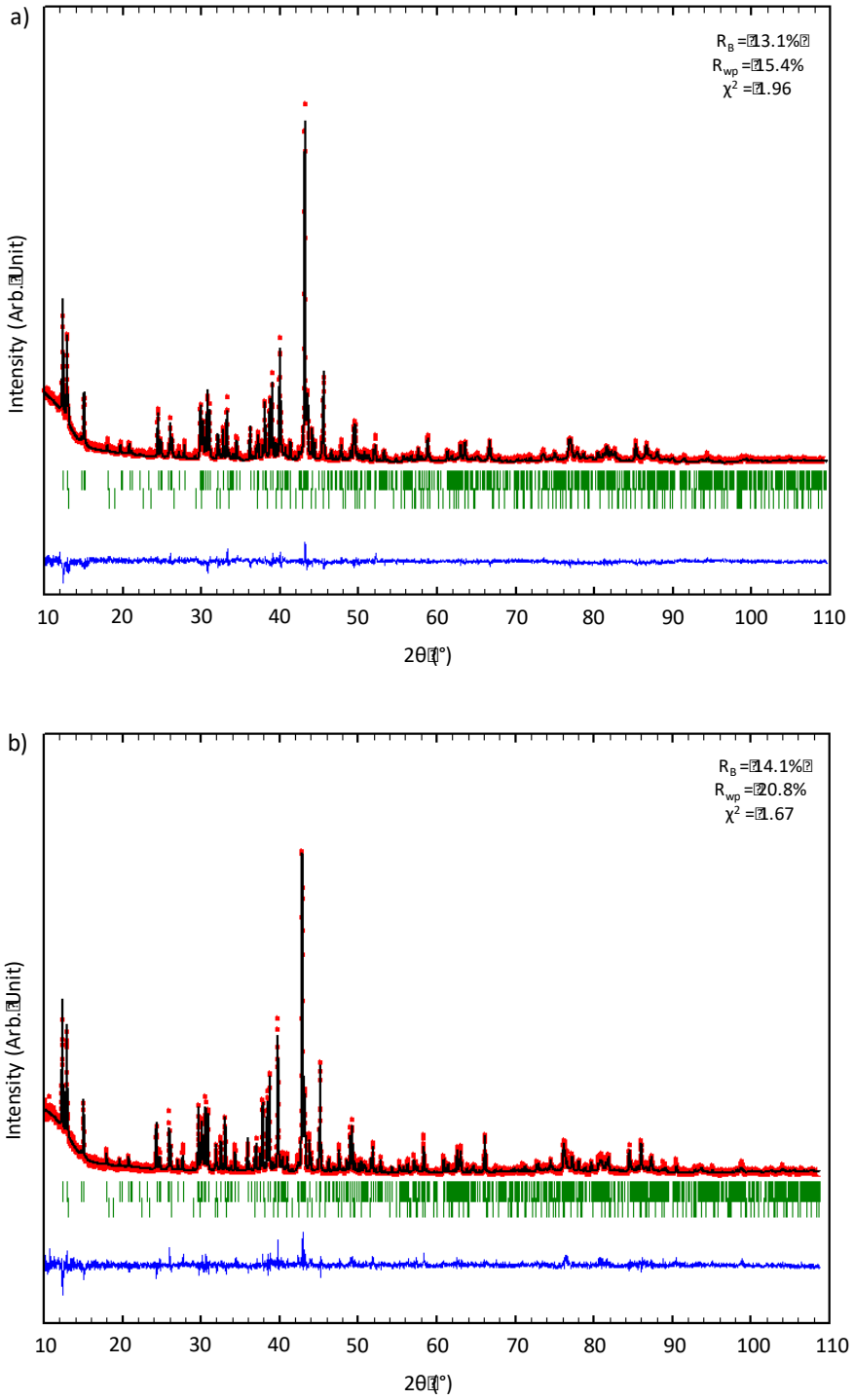
a)
R_B = 13.1%
R_{wp} = 15.4%
χ^2 = 1.96
Intensity (Arb. Unit)
10 20 30 40 50 60 70 80 90 100 110
2θ (°)
b)
R_B = 14.1%
R_{wp} = 20.8%
χ^2 = 1.67
Intensity (Arb. Unit)
10 20 30 40 50 60 70 80 90 100 110
2θ (°)

Figure 2

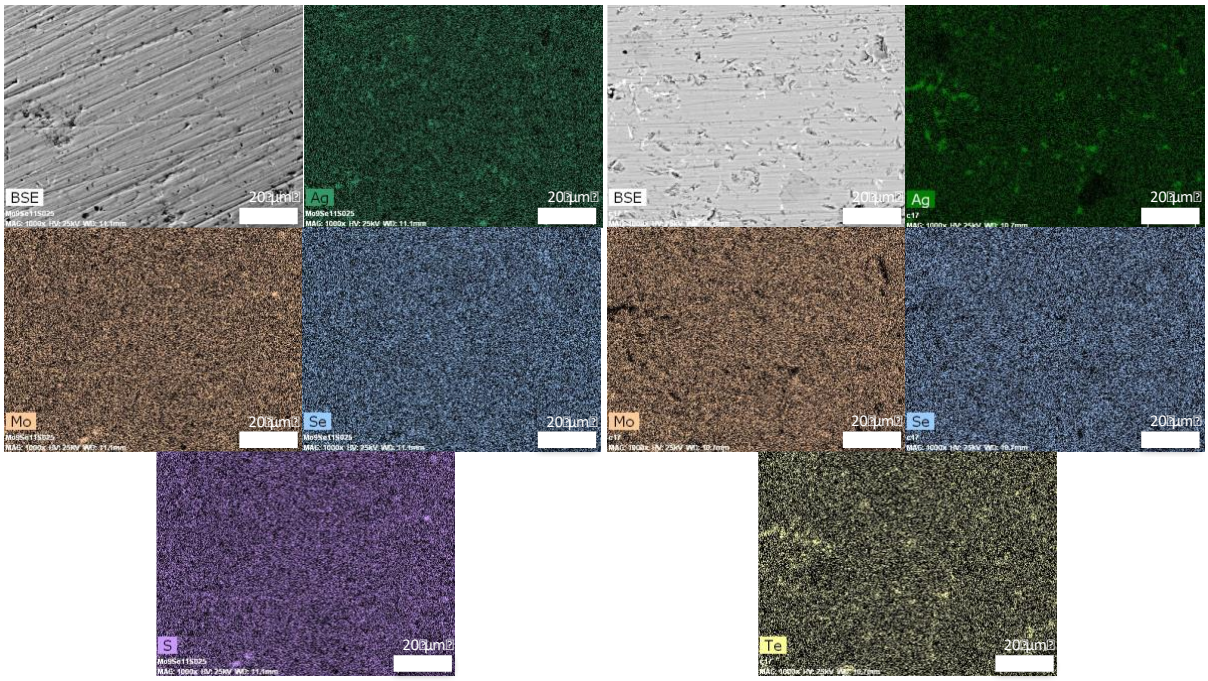

Figure 3

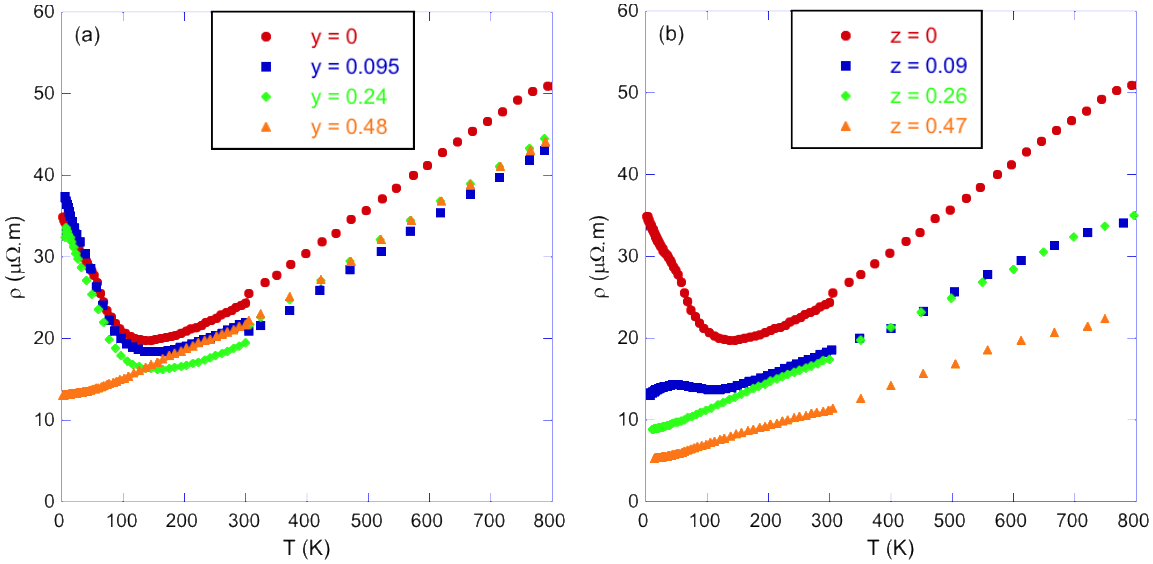

Figure 4

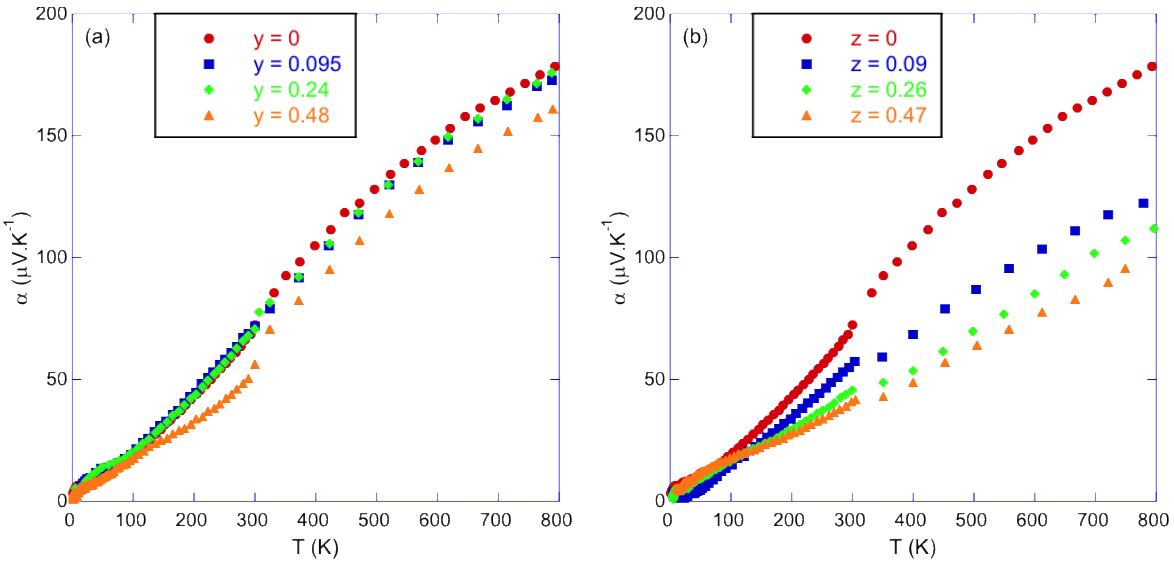

Figure 5

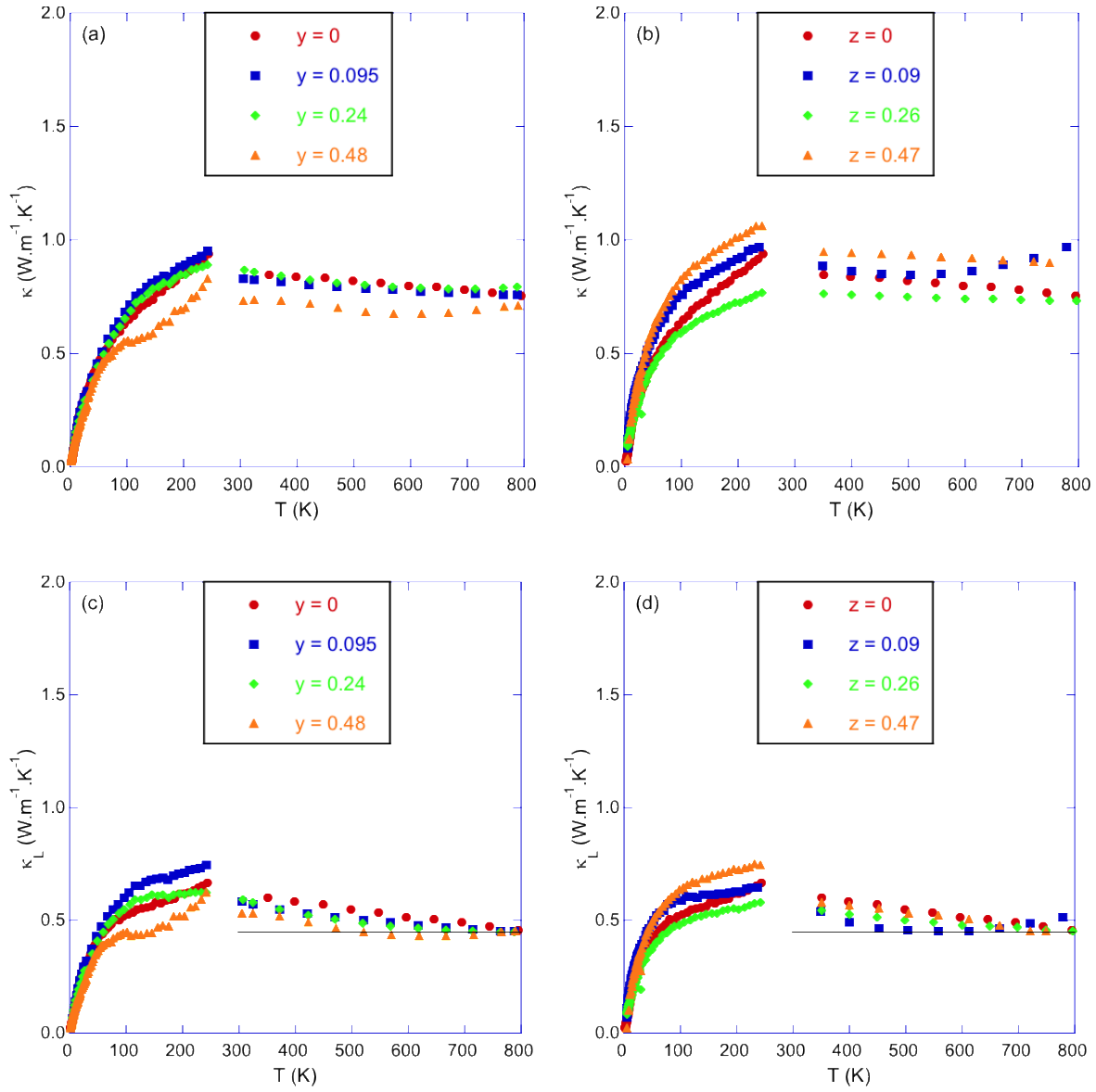
(a)
y = 0
y = 0.095
y = 0.24
y = 0.48
κ (W.m-1.K-1)
T (K)
(b)
z = 0
z = 0.09
z = 0.26
z = 0.47
κ (W.m-1.K-1)
T (K)
(c)
y = 0
y = 0.095
y = 0.24
y = 0.48
κL (W.m-1.K-1)
T (K)
(d)
z = 0
z = 0.09
z = 0.26
z = 0.47
κL (W.m-1.K-1)
T (K)

Figure 6

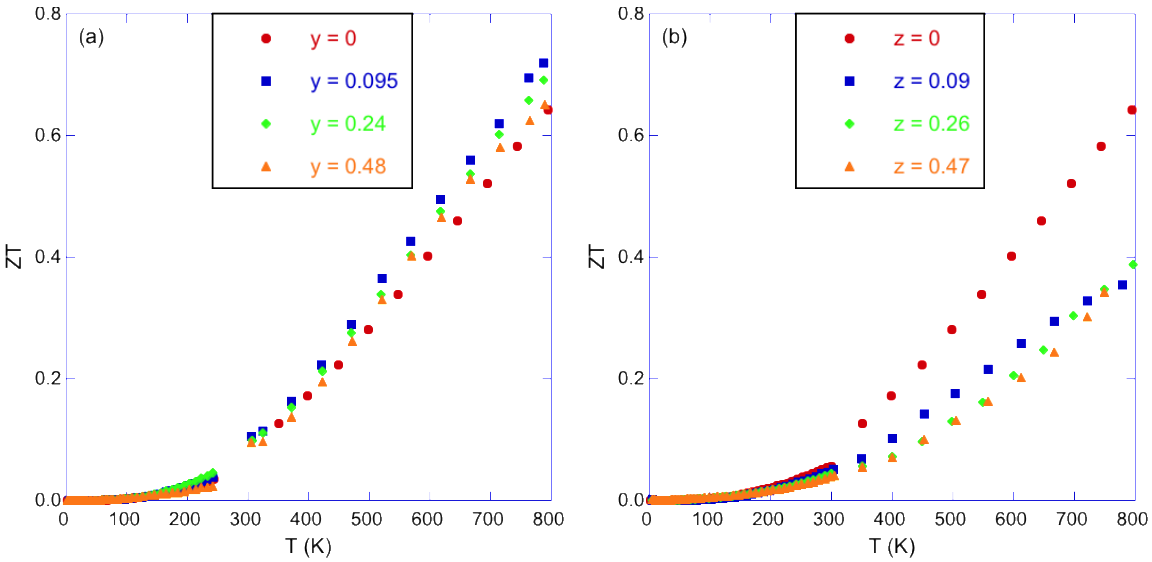

Figure 7